

Article

The Properties of Ultra-High-Performance Concrete with Assembly Unit of Secondary Aluminum Dross and Waste Fly Ash

Houchao Sun ¹, Feiting Shi ¹  and Hui Wang ^{2,*}¹ School of Civil Engineering, Yancheng Institute of Technology, Yancheng 224051, China² School of Civil Engineering and Geographic Environment, Ningbo University, Ningbo 315000, China

* Correspondence: huiwang123@aliyun.com

Abstract: Waste fly ash (WFA) and secondary aluminum dross (SAD) are common solid wastes inducing environmental pollution. These materials contain certain active substances that can be used in cement-based materials. Therefore, cement concrete can be used to solidify these solid wastes. In this study, the influence of the assembly unit of secondary aluminum dross (SAD) and waste fly ash (WFA) on the properties of ultra-high-performance concrete (UHPC) is investigated. The slump flow, the plastic viscosity, the yield shear stress, and the initial setting time of fresh UHPC are measured. Moreover, the flexural and compressive strengths and the dry shrinkage rate (DSR) are determined. The electrical resistance and reactance are tested. The electron microscopy spectroscopy (EDS), thermogravimetric analysis (TG), and X-ray diffraction spectrum (XRD) curves are obtained for revealing the mechanism of macroscopic performances. Results show that due to the optimal specific surface area and the volcanic ash effect, the UHPC with the assembly unit of 50% SAD and 50% WFA provides the highest slump flow, DSR, and mechanical strengths, while the corresponding plastic viscosity, yield shear stress, and electrical resistance are the lowest. The SAD can delay the setting time of UHPC. The relationship between the electrical resistance or the electrical reactance and the mass ratio of SAD accords with the quadratic function. The corresponding electrical resistance is the lowest. The relationship between the mechanical strengths and the electrical resistance fits with the cubic function. The leaching amounts of Z_n and C_r increase in the form of cubic function with the immersing time. Meanwhile, the SAD can decrease the Z_n and C_r by 0%–46.3% and 0%–45.2% respectively. As obtained from the EDS results, the element of Al is increased by adding SAD. The XRD curves show that the crystals of Al_2O_3 are increased and the SiO_2 crystals are decreased by the added SAD. UHPC with 50% SAD exhibits the highest compact microstructures and the least $Ca(OH)_2$ and $3CaO \cdot SiO_2$ hydration products. The TG results show that UHPC with 50% SAD shows the lowest TG values of all the groups. This research will provide new UHPC materials and techniques applied in solidifying the WFA and SAD in the future.



Citation: Sun, H.; Shi, F.; Wang, H. The Properties of Ultra-High-Performance Concrete with Assembly Unit of Secondary Aluminum Dross and Waste Fly Ash. *Coatings* **2024**, *14*, 89. <https://doi.org/10.3390/coatings14010089>

Academic Editor: Valeria Vignali

Received: 10 November 2023

Revised: 8 December 2023

Accepted: 11 December 2023

Published: 9 January 2024

Keywords: secondary aluminum dross; assembly unit; plastic viscosity; electrical resistance; electrical reactance



Copyright: © 2024 by the authors. Licensee MDPI, Basel, Switzerland. This article is an open access article distributed under the terms and conditions of the Creative Commons Attribution (CC BY) license (<https://creativecommons.org/licenses/by/4.0/>).

1. Introduction

To this day, the environmental issues brought by the rapid development of the economy cannot be ignored [1,2]. The waste gas, the liquid waste, and the residue produced from the industrial production have brought serious pollution to the environment [3,4]. Many methods are used for the disposal of waste. However, most current methods for treating waste not only have high costs but also waste considerable amounts of resources. Resource utilization of waste is currently the most concerned topic.

Secondary aluminum dross (SAD) and waste fly ash (WFA) are two kinds of common solid waste. SAD and WFA contain certain amounts of toxic substances and can induce high environmental pollution if the processing method is not appropriate. SAD and WFA

possessing the substances (Al_2O_3 , Fe_xO_y , and CaO) with high cement hydration activity have been applied in the manufacture of cement concrete. The flexural strengths of UHPC can be increased by 23.1% and 28.7% with the additions of SAD and WFA, respectively. However, the corresponding compressive strengths can be increased by 18.7% and 21.3%, respectively [5,6]. Therefore, the use of SAD and WFA in the cement matrix can help the consolidation of their toxic substances. The mechanical strengths and durability of cement concrete can be improved by these two types of solid waste.

According to prior research, the cement materials with SAD show lower mechanical strengths than cement concrete with WFA [7,8]. The flexural and compressive strengths of cement concrete can be increased by SAD with the increasing rates of 0%–27.6% and 0%–18.7%. Meanwhile, the WFA can increase the corresponding flexural and compressive strengths with the increasing rates of 0%–31.6% and 0%–33.2% [9–11]. Furthermore, the cement concrete with WFA demonstrates better mechanical strengths and resistances to freeze–thaw cycles, chloride ion permeability, and corrosion. However, when the WFA is used in the cement concrete, more toxic heavy metal substances seep out of the concrete compared to concrete with SAD, which still pollutes the environment. Therefore, some special methods will be applied to reduce the leaching of toxic substances [12–16]. CO_2 curing on the WFA and its application in ultra-high-performance concrete (UHPC) can help solidify the toxic substances within WFA. The UHPC is made according to the maximum density theory and can prevent the inner toxic substances of WFA from leaching [17,18]. However, the CO_2 curing method is difficult to apply in practical engineering. The use of an assembly unit of SAD and WFA in UHPC can combine the advantages of these two materials [19–22], but little attention has been paid to this.

In this study, the influence of the assembly unit of SAD and WFA on the rheological parameters and the setting time of fresh UHPC is investigated. The electrical resistance and the electrical reactance of UHPC are obtained. The corresponding flexural and compressive strengths are measured. The UHPC's dry shrinkage rate (DSR) is determined. The specimens are cured in the standard curing environment for 28 days. The scanning electron microscopy energy spectrum analysis (SEM-EDS), X-ray diffraction (XRD) spectra, and thermogravimetric analysis (TG) are obtained for the characterization of UHPC products. This research will provide excellent ideas for the resource utilization of these two materials.

2. Materials and Methods

2.1. Raw Materials

Ordinary Portland cement (OPC) from Jiangsu Changlong Cement Manufacturing Co., Ltd., Xuzhou, China with a density of 3.2 g/cm^3 , 117 min initial setting time, and 226 min final setting time is used in this study. Ultra-fine fly ash (FA) with a density of 2.4 g/cm^3 , specific surface area of $312 \text{ m}^2/\text{kg}$, and SiO_2 content higher than 50% is used as a kind of mineral admixture. Blast furnace slag powder (BFP) with a density of 2.8 g/cm^3 , a specific surface area of $434 \text{ m}^2/\text{kg}$, and loss on ignition of 2.2% is used as another kind of mineral admixture. The mineral admixtures are provided by Nanjing Hongqian Environmental Protection Engineering Co., Ltd., Nanjing, China. Beijing Baolaier Technology Co., Ltd., Beijing, China's WFA and Shanghai Haoke Metal Trading Co., Ltd., Shanghai, China's SAD are used in this study. The specific surface areas of SAD and WFA are $345.6 \text{ m}^2/\text{kg}$ and $317.3 \text{ m}^2/\text{kg}$, respectively. The specific surface areas of SAD and WFA are measured with the FBT-9A/9B fully automatic specific surface area tester. The determined data are offered by the manufacturer. Quartz sand provided by Lingshou County Quanfeng Mineral Products Processing Factory, Lingshou, China is used as the aggregate. The particle size ranges are 1 mm–0.5 mm, 0.5 mm–0.1 mm, and 0.1 mm–0.01 mm. Shanxi Kebang Building Materials Co., Ltd., Yuncheng, China's efficient polycarboxylic acid water-reducing agent is used for the adjustment of the fresh UHPC's fluidity. The accumulated pass rates and the chemical compositions of the raw materials are exhibited in Tables 1 and 2 respectively.

Table 1. The accumulated pass rate (%).

Types	Particle Size/ μm						
	0.3	0.6	1	4	8	64	360
OPC	0.12	0.37	3.09	14.77	29.14	92.61	100
FA	32.04	59.01	82.99	99.8	99.9	100	100
QS	0	0	0	0	0.036	23.95	100
SAD	0.039	0.31	0.55	1.10	3.94	25.35	88.13
WFA	0.13	0.51	2.29	17.36	31.14	97.10	100

Table 2. Chemical composition (%).

Types	SiO ₂	Al ₂ O ₃	Fe _x O _y	MgO	CaO	SO ₃	K ₂ O	Na ₂ O	TiO ₂	Loss on Ignition
OPC	20.2	5.7	3.8	1.8	62.3	2.9	-	-	-	3.0
FA	90.1	0.3	0.6	0.3	0.45	0.2	7.4	-	-	-
QS	98.4	-	1.4	-	-	-	-	-	-	-
SAD	4.6	78.9	4.4	5.1	1.7	-	-	0.9	-	-
WFA	22.3	4.5	0.8	-	20.1	9.5	5.9	4.4	10.1	21.1

2.2. The Preparing of Specimens

Table 3 shows the mixing proportions of UHPC. The mixing proportions are obtained from the maximum density theory referring to references [6,23]. The UHPC specimens are prepared via the following steps. The powder binder materials are poured from Xianxian Longhui Highway and Railway Test Instrument Factory, Xi'an, China's JJ-5 planetary cement mortar mixer and mixed at a stirring speed of 140 rpm for 30 s. Then, the quartz sand is poured, and 285 rpm stirring is provided to the materials for 90 s. Finally, the water mixed with water reducing agent is added to the mixture, and 120 s stirring with a speed of 285 rpm is offered for the mixture.

Table 3. The mixing proportions of UHPC (kg/m³).

Water	OPC	SAD	WFA	FA	QS	WR
240.2	657.9	0	364.0	182.0	961.5	16.0
240.2	657.9	91.0	273.0	182.0	961.5	16.0
240.2	657.9	182.0	182.0	182.0	961.5	16.0
240.2	657.9	273.0	91.0	182.0	961.5	16.0
240.2	657.9	364.0	0	182.0	961.5	16.0

2.3. Experimental Aim and Methodology

2.3.1. Experimental Aim

The rheological parameters of fresh UHPC are of great significance for its construction performance. The fresh UHPC's slump flow, plastic viscosity, and yield shear stress are commonly used to characterize its rheological properties. The mechanical strengths of UHPC are its most important parameters and can reflect the reasonableness of the mixing proportions. The electrical resistance and reactance of UHPC can reflect the mechanism of mechanical properties. Electrical resistance can be used as a non-destructive method of characterizing their mechanical strengths. The UHPC's dry shrinkage rate (DSR) can reflect its cracking performance. The scanning electron microscopy energy spectrum analysis (SEM-EDS), X-ray diffraction (XRD) spectra, and thermogravimetric analysis (TG) in this research are obtained to further reflect the intrinsic mechanism of UHPC performance. Consequently, these performance parameters need to be measured in this article.

2.3.2. Experimental Methodology

The Measurement of Rheological Parameters and Initial Setting Time

The jumping table method is applied in the measurement of slump flow. An HLB-2 Mobile Concrete Rheometer with a mixing speed of 0 rpm–30 rpm is used for the measurement of the plastic viscosity and yield shear stress of fresh UHPC. The measuring temperature and humidity for the measurements of rheological parameters are kept at 20 °C and 50%, respectively since the rheological properties of the fresh UHPC are greatly affected by the temperature and the humidity. Generally, the construction environment and the conditions for preparing commercial concrete are close to room environments. Therefore, the environment of room temperature and humidity is used as the testing condition for rheological parameters. The measuring details are shown in References [24–26]. Figure 1 shows the measurements of the fresh UHPC's slump flow, yield shear stress, and plastic viscosity.

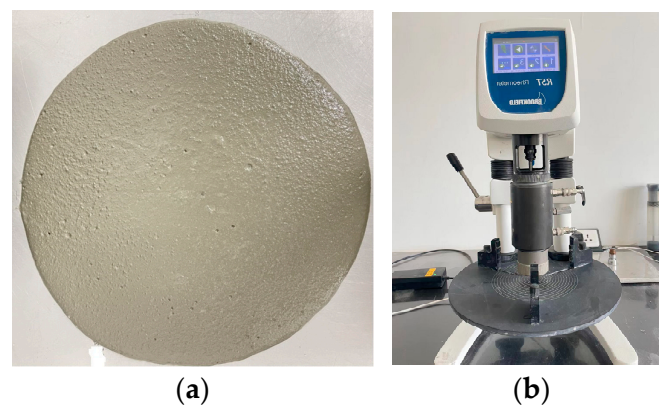


Figure 1. The measurement of rheological parameters. (a) The measurement of slump flow; (b) the rheometer for measuring the UHPC's rheological parameters.

Cangzhou Qiuzhen Instrument Equipment Co., Ltd., Cangzhou, China's digital display mortar setting time tester is used for measuring the initial setting time of fresh UHPC, as shown in Figure 2.



Figure 2. The measurement of initial setting time.

The Measurement of Electrical Parameters

A TH2816B electrical digital bridge (Suzhou Xintonghui Electronics Co., Ltd., Suzhou, China) with the voltage of 2 V and the testing frequency of 10^5 Hz is used for the measurement of AC electrical resistance. The electrical reactance of UHPC is measured with a Wellington RST5060F Electrochemical Workstation offered by Gongyi Honghua Instrument Equipment Industry and Trade Co., Ltd., Gongyi, China and is also used to obtain the AC impedance spectrum (Figure 3). The electrical frequency ranges from 10^5 Hz to 1 Hz, and the testing voltage is -10 mV– 10 mV. The electrical reactance is measured at the AC electri-

cal frequency of 10^5 Hz for the reason that electrical voltage with a higher frequency shows higher stability and accuracy of electrical parameters just obtained from reference [27].

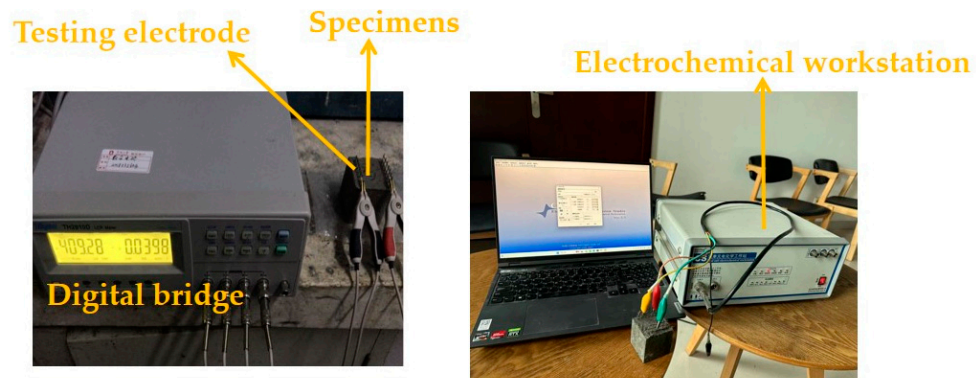


Figure 3. The measurement of electrical parameters.

The Measurement of Mechanical Strengths and Drying Shrinkage Rate

In this study, all specimens are cured in a standard curing environment (temperature of 20 ± 2 °C and humidity of 98.3%). The fully automatic bending integrated testing machine is used to measure the flexural and compressive strengths. The loading rates of 0.05 kN/s and 2.4 kN/s, respectively, are provided. The mechanical strengths are carried out with specimens sized $40 \times 40 \times 160$ mm³. The specimens are placed on the flexural clamp and loaded to destruction. After that, the two half-specimens are moved to the compressive clamp and loaded to destruction. The mechanical strengths of specimens are measured at a temperature of 20 °C and a humidity of 50% (Figure 4).



The measurement of flexural strength **The measurement of compressive strength**

Figure 4. The measurements of mechanical strengths.

The drying shrinkage rate (*DSR*) is determined via the following steps (Figure 5). Samples are fixed on a bracket with the dial indicator at the center after specimens' hardening and demolding. The initial lengths (L_0) of the samples are measured when they are preliminarily installed. When the planned curing age is reached, the length (L_t) of the specimen is tested again. The *DSR* can be obtained using Equation (1).

$$DSR = \frac{L_t - L_0}{L_0} \quad (1)$$



Figure 5. The testing process of DSR.

The Measurement of Leached Toxic Element

Specimens with sizes of $100 \times 100 \times 100 \text{ mm}^3$ are used for determining the leached toxic heavy metal substances during immersion in the deionized water for 6 months. The deionized water is taken out for measurement of heavy metal ions. Six samples are tested for each specimen. The immersed C_r and Z_n in the deionized water are measured per month using an Inductively Coupled Plasma Emission Spectrometer (Shanghai Meishan Instrument Co., Ltd., Shanghai, China). The scanning wavelength range and relative standard deviation are 185 nm–435 nm and lower than 1.5%, respectively. The flowchart of all experimental processes is shown in Figure 6.

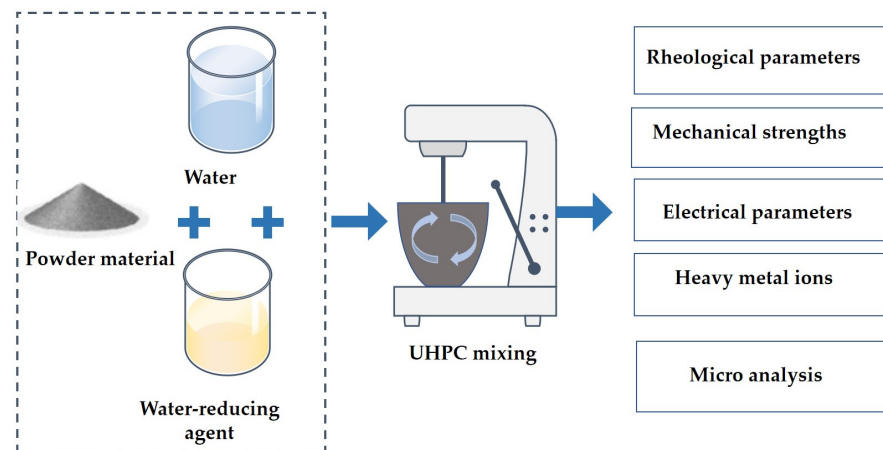


Figure 6. The flowchart of all experimental processes.

Microscopic Research Measurement

An SU3800 scanning electron microscope purchased from Shanghai Weihai Optoelectronic Technology Co., Ltd., Shanghai, China is used for obtaining the SEM photos and EDS results. All the samples are removed from the core of the specimens. Then, the samples are dried in the oven at a temperature of 105 °C for 2 days. After that, the samples are disposed of with vacuum gold spraying. Finally, the sprayed samples are moved to the SU3800 scanning electron microscope for SEM and EDS measurements.

The samples are ground into powder and then used for the measurement of X-ray diffraction curves by the Bruker JV-DX X-ray diffractometer provided by Shanghai Erdi

Instrument Technology Co., Ltd., Shanghai, China. Moreover, some powder is used for thermogravimetric analysis using the TGA thermogravimetric analyzer provided by Shanghai Farui Instrument Technology Co., Ltd., Shanghai, China.

3. Results and Discussions

3.1. The Rheological Parameters of UHPC

The slump flow of fresh UHPC is shown in Figure 7. The slump flow of fresh UHPC increases from 213.1 mm to 234.6 mm, with the SAD's mass ratio increasing from 0% to 50% corresponding to the WFA ranging from 100% to 50%. The increasing rate of the slump flow ranges from 0% to 10.3%. The SAD shows a higher ball effect than that of WFA, which increases the slump flow of fresh UHPC, just as found in References [28,29]. However, when the SAD mass ratio is higher than 50%, the slump flow of fresh UHPC decreases from 234.6 mm to 224.5 mm. It can be observed in Section 2.1 that the SAD possesses larger specific surface area than the WFA, leading to more adsorption of free water [8]. Therefore, the slump flow shows a decreasing trend with the addition of SAD higher than 50%. The error bars' values are lower than 3.3% of the slump flow, indicating the accuracy of experimental data.

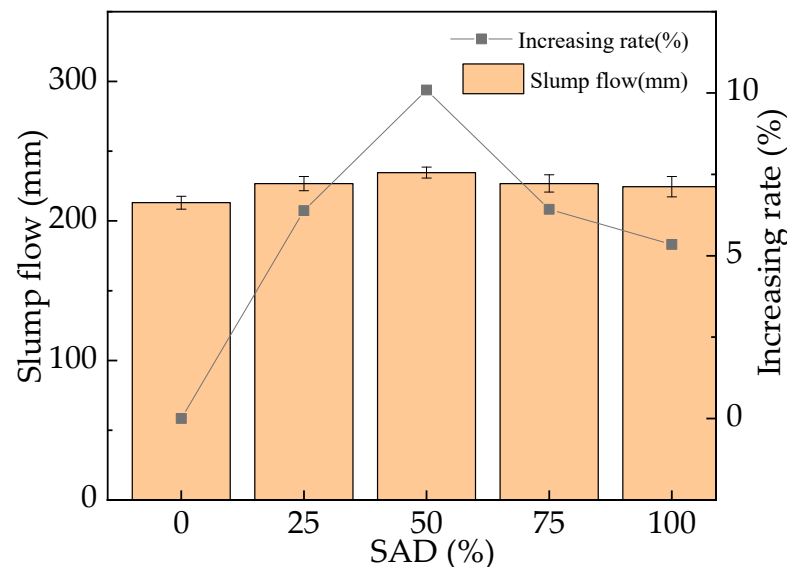


Figure 7. The slump flow of fresh UHPC with different dosages of SAD.

Figure 8 shows the plastic viscosity of fresh UHPC. The plastic viscosity decreases from 13.1 Pa·s to 10.7 Pa·s with the SAD dosage increasing from 0% to 50% corresponding to the WFA ranging from 100% to 50%. However, when the SAD ranges from 50% to 100%, the plastic viscosity of fresh UHPC increases from 10.7 Pa·s to 11.7 Pa·s. It can be observed from prior research that the rotational plastic viscosity values of freshly mixed cement-based materials are inversely correlated with their slump flow [30]. When the SAD increases from 0% to 50%, the slump flow increases, just as observed in Figure 6. Therefore, the plastic viscosity of fresh UHPC decreases. Meanwhile, the slump flow of UHPC decreases with the adding SAD increasing from 50% to 100%, resulting in an increase in plastic viscosity. The varying rate of the plastic viscosity firstly decreases from 0% to -17.3% and then increases from -17.3% to -10.3% . The plastic viscosity of fresh UHPC shows the maximum error bars of 8.40% of the plastic viscosity, ensuring the experimental data's accuracy.

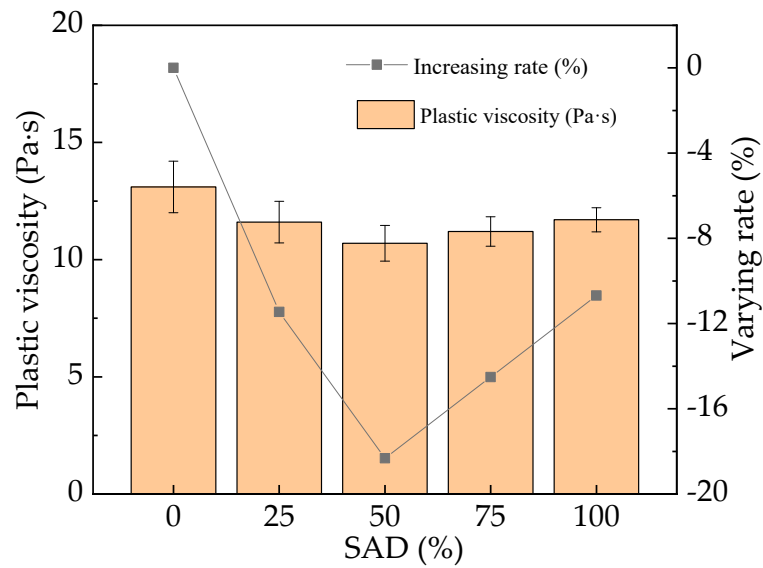


Figure 8. The plastic viscosity of fresh UHPC with different dosages of SAD.

The yield shear stress of fresh UHPC is shown in Figure 9. The yield shear stress varies according to a similar rule to that of fresh UHPC’s plastic viscosity which is the same as that of fresh UHPC’s plastic viscosity. When the dosage of SAD is 50%, the yield shear stress reaches the minimum value. The lowest yield shear stress and the varying rate are 21.3 Pa and 18.2%. The maximum error bar’s value is 8.05% of the yield shear stress, confirming the accuracy of the experimental result.

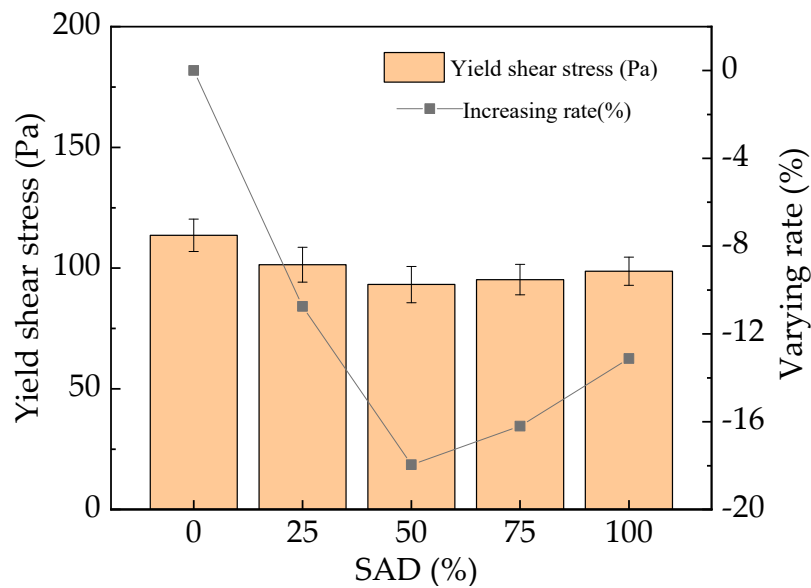


Figure 9. The yield shear stress of fresh UHPC with different dosages of SAD.

3.2. The Initial Setting Time of UHPC

Figure 10 shows the initial setting time of fresh UHPC. The initial setting time increases from 178 min to 225 min. The fact that the volcanic ash reaction of SAD is lower than that of WFA leads to delay in the setting of cement [31,32]. It can be observed in Figure 10 that the increasing rate of the initial setting time is 0%–26.7%. The error bars’ values are 0%–0.9% of the initial setting time’s values, indicating the experimental correctness.

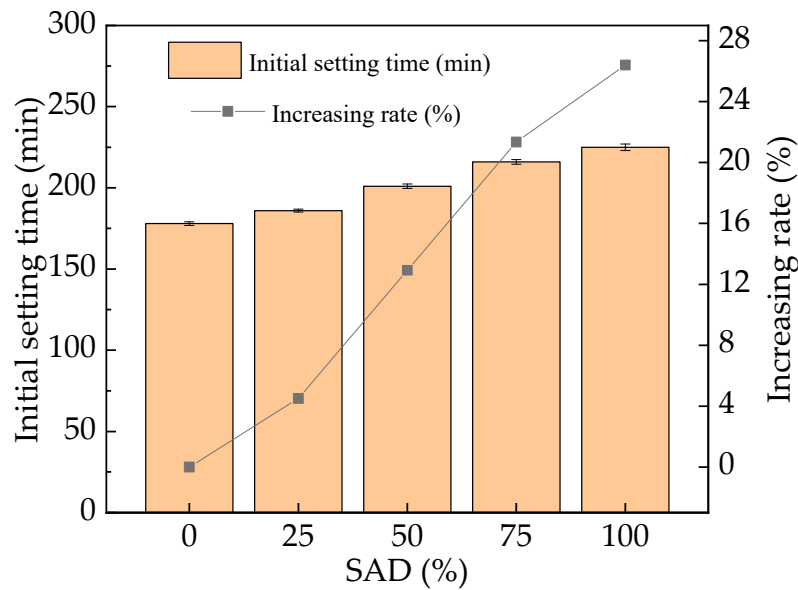


Figure 10. The initial setting time of fresh UHPC with different dosages of SAD.

3.3. The DSR of UHPC

The DSR of UHPC is shown in Figure 11. The DSR of UHPC firstly increases from $386 \times 10^{-6}\%$ to $428 \times 10^{-6}\%$, with the mass ratio of SAD increasing from 0% to 50%. This is because the SAD possesses greater specific surface area than the WFA, which can accelerate the hydration speed of UHPC [33]. Therefore, the hydration speed of UHPC is increased by adding SAD, thus accelerating the hydration degree of UHPC. When the added SAD increases from 50% to 100%, the DSR decreases from $428 \times 10^{-6}\%$ to $398 \times 10^{-6}\%$. This is because the SAD shows a lower pozzolanic effect than the WFA, leading to lower hydration activity and decreased DSR [34]. The rate of increase of DSR is 11.3%. The error bars' values are 2.67%~5.51% of the DSR values, which ensures the accuracy of the experimental results. Compared to prior studies on SAD- and WFA-blended UHPC, UHPC with an assembly unit of WFA and SAD shows higher DSR than the UHPC with SAD and lower DSR than the UHPC with WFA [35].

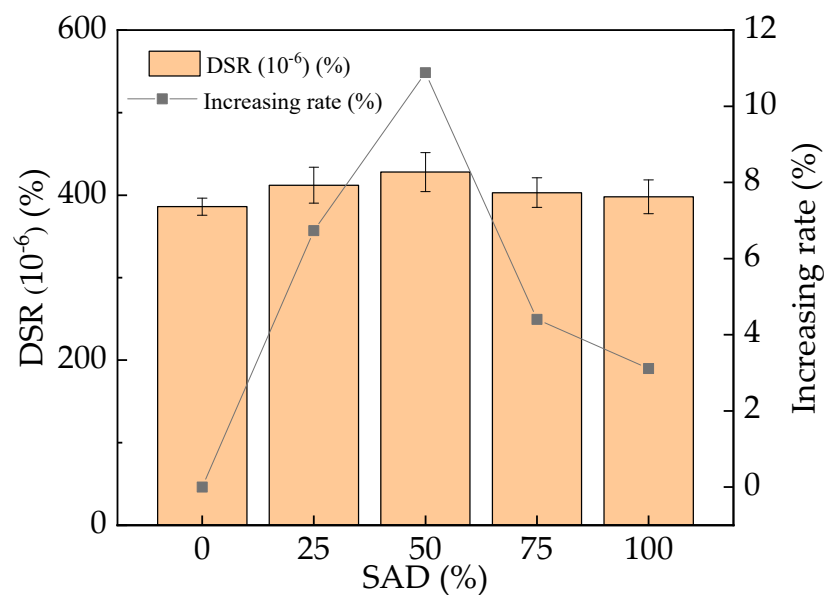


Figure 11. The DSR of UHPC with different dosages of SAD.

3.4. The Electrical Reactance of UHPC

The electrical reactance, whose unit is picofarad (pF), of UHPC is illustrated in Figure 12. It can be observed that the electrical reactance ranges from 13,261 pF to 25,123 pF with an increasing rate of 0%–89.5%. The UHPC is composed of multiple components (pore solutions, gel, and crystals). The interface between different substances causes an increase in capacitance value. The capacitance will generate a reverse electric field in UHPC, resulting in a decrease in the electrical conductivity. The SAD can increase the electrical reactance of UHPC. The electrical reactance of UHPC demonstrates a quadratic function with the mass ratio of SAD. The SAD possesses greater specific surface area than WFA, therefore, the interfaces between different phases are higher, leading eventually to increasing the electrical reactance of UHPC [36,37]. The fitting degree of the function from the fitting of the SAD's mass ratio and the electrical reactance is 0.92, ensuring the rationality of the fitting results.

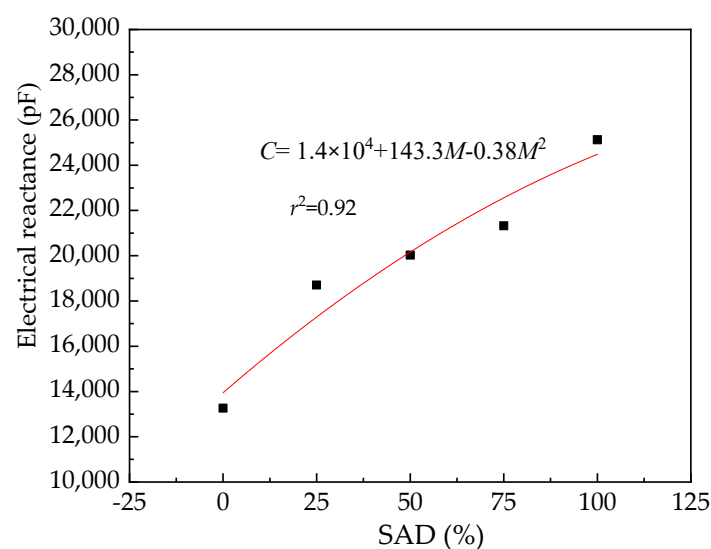


Figure 12. The electrical reactance of UHPC with different dosages of SAD.

3.5. The Electrical Resistance of UHPC

The electrical resistance of UHPC is exhibited in Figure 13. The electrical resistance of UHPC shows the quadratic function with the mass ratio of SAD. When the SAD mass ratio is 50%, the electrical resistance is the lowest. The fitting degree is 0.91, indicating the reasonability of fitting equations. The SAD possesses a greater amount of metallic oxide than the WFA. Therefore, more free electrons exist in UHPC. Therefore, the electrical resistance of UHPC decreases with the increasing dosages of SAD [38,39]. However, when the SAD content is higher than 50%, the increased electrical reactance of SAD (as shown in Figure 12) results in the decreased electrical conduction and the increased electrical resistance of UHPC.

3.6. The Mechanical Strength of UHPC

The flexural and compressive strengths of UHPC are shown in Figure 14. The flexural and compressive strengths of UHPC firstly increase and then decrease, with the increasing SAD dosages ranging from 0% to 50%. The SAD shows higher specific surface area, leading to an increase in the degree of hydration and an increase in mechanical strength. However, when the SAD amount ranges from 50% to 100%, the mechanical strength shows a downward trend with the increasing mass ratio of SAD. As noted in Refs. [40,41], the SAD shows a lower volcanic ash effect than the WFA, and the UHPC with WFA can hydrate more completely. Therefore, when the added SAD dosage is higher than WFA, the UHPC

exhibits decreased mechanical strength. As shown in Figure 13, UHPC with 50% SAD shows the highest mechanical strengths.

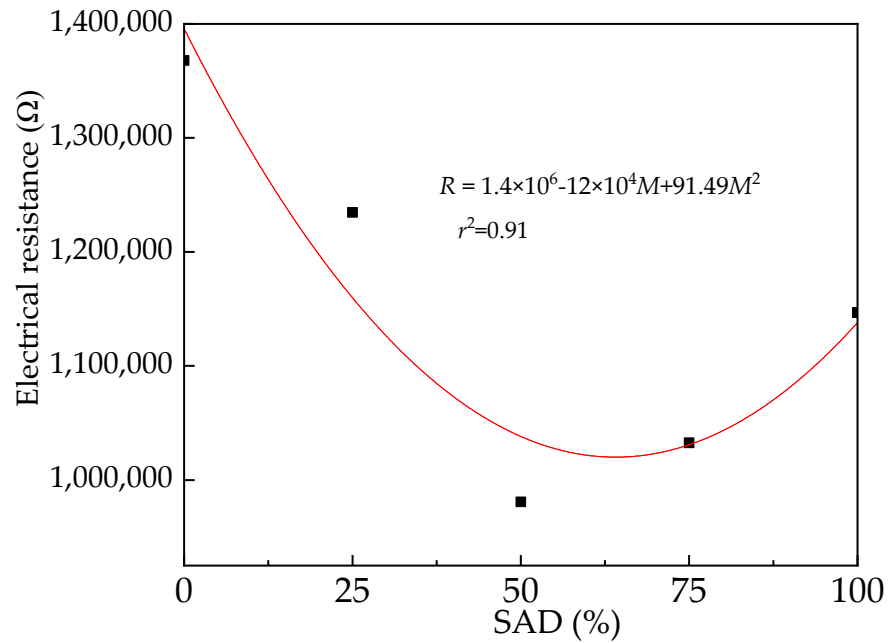


Figure 13. The electrical resistance of UHPC with different dosages of SAD.

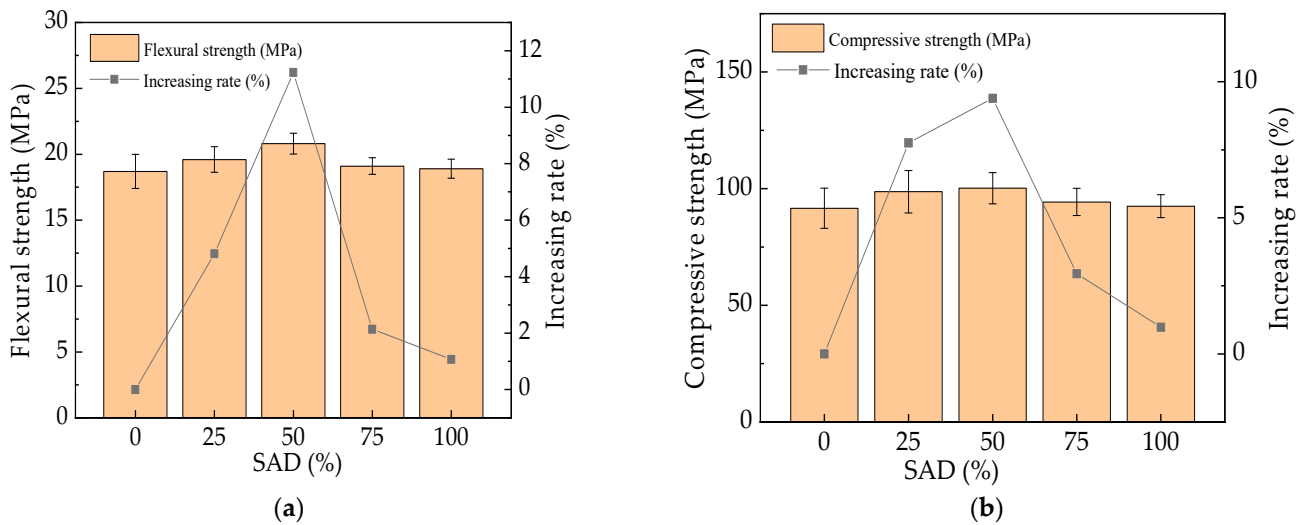


Figure 14. The mechanical strengths UHPC with different dosages of SAD. (a) The flexural strength; (b) the compressive strength.

The fitting results of the relationship between the mechanical strengths and the electrical resistance are shown in Figure 15. The fitting curves coincide with the cubic function. The SAD contains some aluminum oxide, showing the improved electrical conduction. The mechanical strengths are closely related to the hydration of cement in UHPC [42,43]. The dosages of SAD can affect the hydration degree and the electrical conduction of UHPC. Hence, an inherent law between the electrical resistance and the mechanical strengths of UHPC exists. As shown in Figure 15, the fitting degrees are higher than 0.95, verifying the accuracy of the fitting equation.

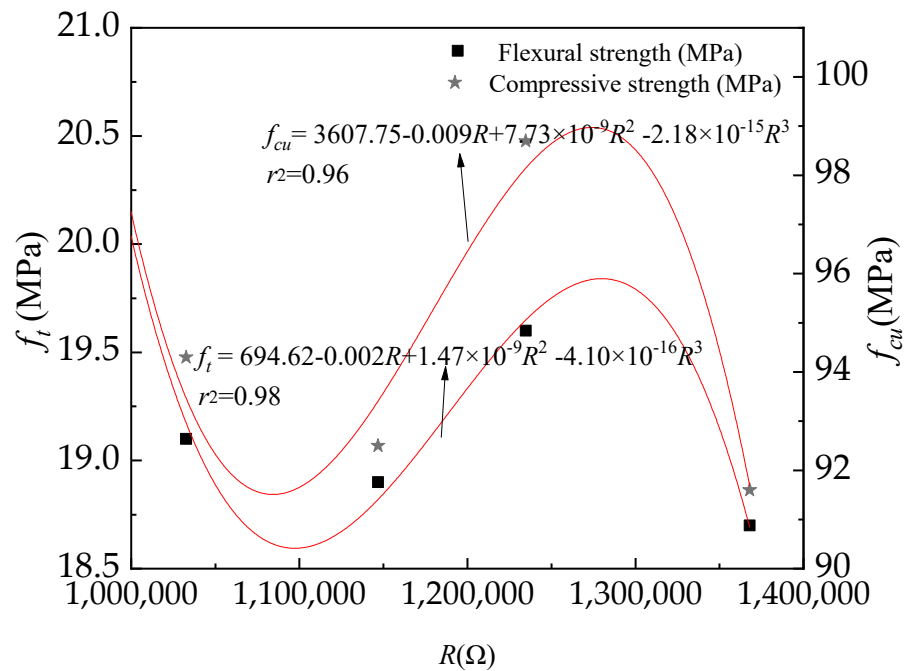
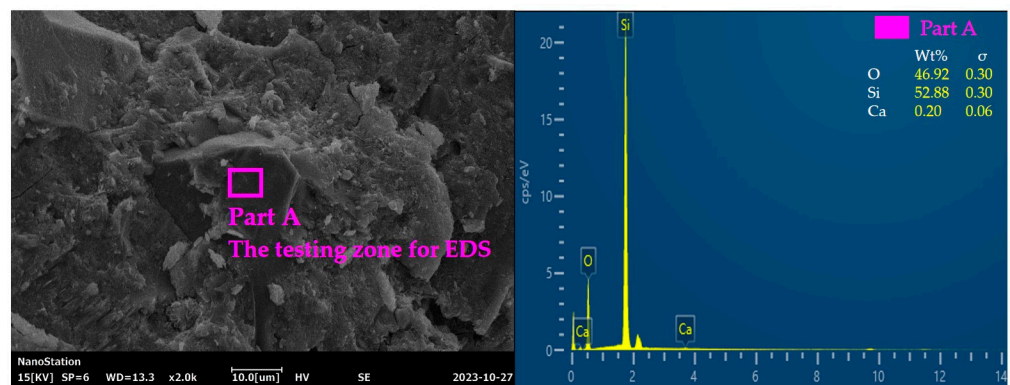


Figure 15. The fitting curves between mechanical strengths and the electrical resistance.

Figure 16 shows the SEM-EDS photos of UHPC. Figure 16 indicates that the UHPC consists of flocculent and needle-shaped hydration products. The flocculent hydration products are evenly dispersed in UHPC. When the dosages of SAD increase from 0% to 50%, the needle-shaped hydration products are increased and the cracks are decreased, leading to more compact micro-structures. However, when the mass ratio of SAD varies from 50% to 100%, the loose hydration products are increased and the compact hydration products are decreased, resulting in more loose micro-structures. The research results of SEM photos have confirmed that the SAD lower than 50% can improve the mechanical strengths of UHPC. UHPC with SAD higher than 50% demonstrates a negative effect on mechanical performance. It can be observed in Figure 16, that the elements O, Si, and Ca are found in Figure 16a. The elements O, Ca Na, Al, K, and Fe are observed in Figure 16b. Finally, the elements C, O, Mg, Al, and Ca are discovered in Figure 16c. It can be seen in Figure 16 that the increased dosages of SAD lead to increases in Al in the UHPC, which stems from the Al element in SAD.



(a)

Figure 16. Cont.

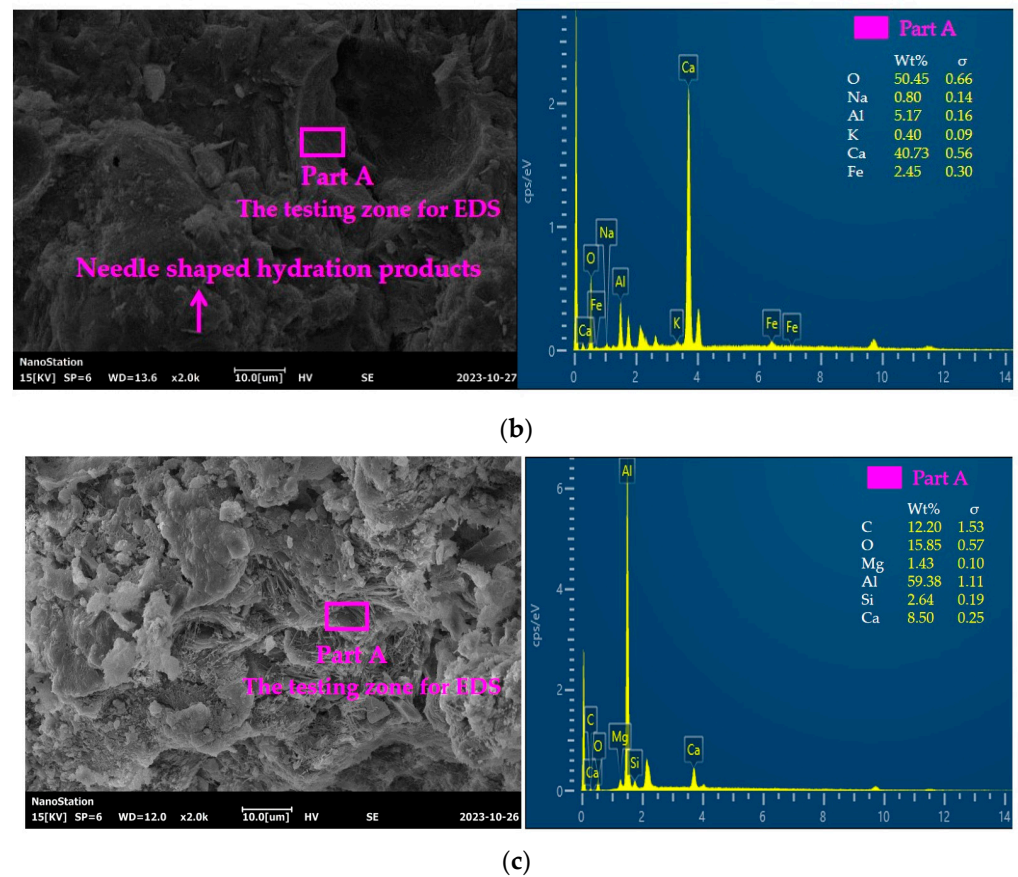


Figure 16. The EDS of UHPC. (a) UHPC with 0% SAD; (b) UHPC with 50% SAD; (c) UHPC with 100% SAD.

TG is a thermal analysis technique that measures the relationship between the sample's mass and the variation of temperature under the program-controlled temperature, applied in analyzing the thermal stability and composition of materials. The TG curves of UHPC are shown in Figure 17. The TG curves of UHPC are separated into three parts. In the first part, the temperature ranges from 21.3 °C to 151.3 °C, and the TG values decrease from 100% to 96.7%, which is induced by the evaporated free water. The TG values decrease from 96.7% to 85.7% as the temperature increases from 151.3 °C to 407.6 °C due to the decomposition of calcium silicate hydrate (C-S-H) hydration products. Finally, the TG declines from 87.3% to 80.1%, with the increasing temperature from 407.6 °C to 713.2 °C. This is ascribed to the decomposed $\text{Ca}(\text{OH})_2$ (CH) hydration products. The TG values are decreased by adding SAD ranging from 0% to 50%, due to the increased C-S-H hydration products. When the SAD increases from 50% to 100%, the TG values corresponding to 407.6 °C–713.2 °C increase, which is ascribed to the increased CH.

The XRD images of UHPC are shown in Figure 18. All the samples are cured for 28 days. From Figure 18, the diffraction peaks of SiO_2 , Al_2O_3 , CH, $3\text{CaO}\cdot\text{SiO}_2$ (C3S), $2\text{CaO}\cdot\text{SiO}_2$ (C2S), and hydrate calcium silicate (C-S-H) are found. When the mass ratio of SAD increases from 0% to 50%, the diffraction peaks of CH are increased, which indicates the decreased CH crystallinity and the increased secondary hydration of cement. However, when the mass ratio of SAD increases from 50% to 100%, the diffraction peaks of CH are increased, indicating increased CH crystallinity and a reduction in secondary hydration. UHPC with 50% SAD shows the least CH and C3S crystallinity. The XRD results confirm that the UHPC with 50% SAD shows the best mechanical properties.

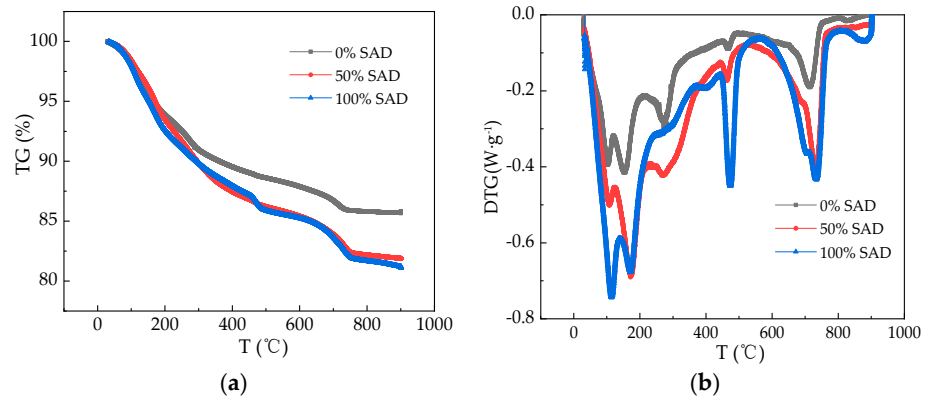


Figure 17. The TG analysis of UHPC. (a) The TG curves of UHPC; (b) the DTG curves of UHPC.

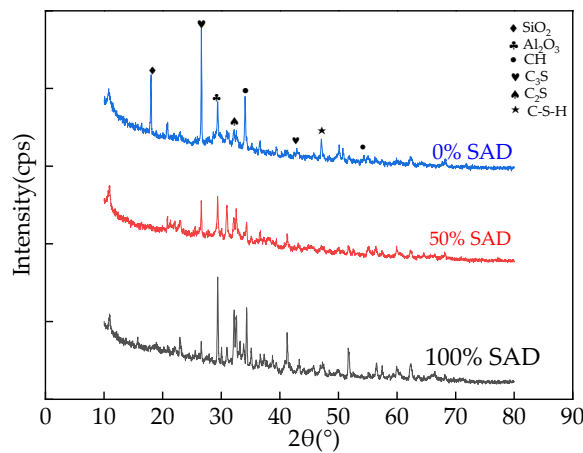


Figure 18. The XRD curves of UHPC.

3.7. The Leaching of C_r and Z_n

The leaching of C_r and Z_n are shown in Figure 19. The fitting results of the relationship between the leaching amount of toxic heavy metal elements and the immersion time is shown in Table 4. It is shown in Figure 19 and Table 4 that the leached C_r and Z_n increase in the form of a cubic function. Due to the reason that the WFA possesses some amount of C_r and Z_n. Therefore, the amounts of C_r and Z_n increase with the immersion time. Moreover, the added SAD decreases the C_r and Z_n by 0%–93.6% and 0%–96.1%, respectively. This is because the WFA possesses a higher amount of C_r and Z_n than the SAD. Consequently, the UHPC with more SAD shows a lesser amount of toxic metals.

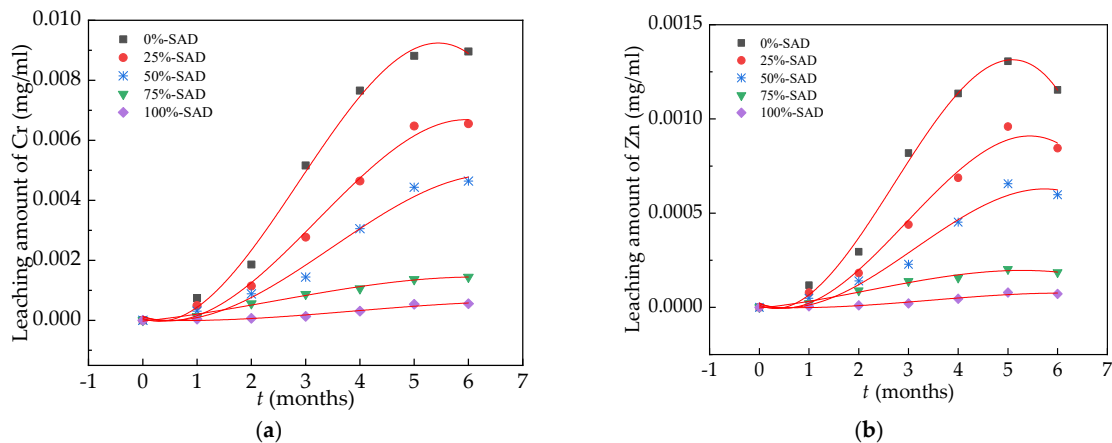


Figure 19. The leached toxic substances. (a) The leaching amount of C_r; (b) the leaching amount of Z_n.

Table 4. The fitting results of the relationship between the leaching amount of toxic heavy metal elements and the immersion time.

Equation	Types	<i>a</i>	<i>b</i>	<i>c</i>	<i>d</i>	R ²
$C_r = at^3 + bt^2 + ct + d$	0%-SAD	-1.36×10^{-4}	0.0012	-6.71×10^{-4}	6.80×10^{-5}	0.99
	25%-SAD	-8.13×10^{-5}	7.83×10^{-4}	-6.82×10^{-4}	1.36×10^{-4}	0.99
	50%-SAD	-4.61×10^{-5}	4.82×10^{-4}	-4.53×10^{-4}	1.11×10^{-4}	0.97
	75%-SAD	-7.91×10^{-6}	5.77×10^{-5}	1.83×10^{-4}	-2.46×10^{-5}	0.98
	100%-SAD	-5.04×10^{-6}	5.86×10^{-5}	-7.71×10^{-5}	2.07×10^{-5}	0.94
$Z_n = at^3 + bt^2 + ct + d$	0%-SAD	-2.42×10^{-5}	1.97×10^{-4}	-1.19×10^{-4}	1.28×10^{-5}	0.99
	25%-SAD	-1.51×10^{-5}	1.34×10^{-4}	-1.19×10^{-4}	2.32×10^{-5}	0.97
	50%-SAD	-8.95×10^{-6}	8.41×10^{-5}	-8.15×10^{-5}	1.89×10^{-5}	0.95
	75%-SAD	-1.77×10^{-6}	1.16×10^{-5}	2.60×10^{-5}	-3.47×10^{-6}	0.97
	100%-SAD	-1.02×10^{-6}	1.04×10^{-5}	-1.38×10^{-5}	3.30×10^{-6}	0.91

4. Conclusions

The conclusions are obtained from the research results and summarized as follows.

The slump flow of fresh UHPC reaches its highest (234.6 mm), when the mass ratio of SAD is 50%. The maximum increasing rate of the fresh UHPC's slump flow is 10.3%. The plastic viscosity and the yield shear stress of fresh UHPC with 50% SAD reach the minimum values of 10.7 Pa·s and 21.3 Pa, respectively, while the corresponding maximum increasing rates are 17.3% and 18.2%, respectively.

SAD has a retarding effect on the fresh UHPC and can increase the initial setting time by 0%–26.7%. UHPC with 50% SAD shows the highest DSR, with an increasing rate of 11.3%.

The electrical resistance and reactance vary in the form of quadratic function with the mass ratio of SAD. UHPC with 50% SAD shows the lowest electrical resistance. The SAD produces a positive effect on the electrical reactance of UHPC.

The mechanical strengths are increased by adding SAD with the dosages of 0%–50%. When the SAD mass ratio increases from 50% to 100%, the corresponding effect on mechanical strength is negative. The relationship between electrical resistance and mechanical strength is coincident with the cubic function. Due to the optimal specific surface area and the volcanic ash effect, UHPC with 50% SAD shows the highest compactness and the optimum mechanical strength.

The addition of SAD can increase Al content. Moreover, the SAD increases crystals of Al₂O₃ and decreases SiO₂ crystals. UHPC with 50% SAD exhibits the highest compact microstructures and the least CH and C3S hydration products. At this moment, the hydration degree is the highest.

This paper has found the optimum mixing proportions of UHPC with the assembly unit of WFA and SAD. Simultaneously, various performance indicators—including the rheological properties, the mechanical properties, the electrical properties, and the microscopic properties of this type of UHPC—have been obtained. The electrical resistance of the UHPC can be used to calculate its mechanical strengths. This research will provide new materials and technology for the solidification of solid waste in the future.

Author Contributions: Software, H.S., F.S. and H.W.; Validation, H.S. and H.W.; Formal analysis, H.S. and F.S.; Investigation, H.S. and F.S.; Writing—original draft, H.S.; Writing—review & editing, H.W.; Funding acquisition, H.W. All authors have read and agreed to the published version of the manuscript.

Funding: This research was funded by Zhejiang Provincial Natural Science Foundation, grant number [LY22E080005], and Ningbo Natural Science Foundation Project, grant number [2023J086], and Horizontal Project Contract, grant number [No. YG20211111205].

Institutional Review Board Statement: Not applicable.

Informed Consent Statement: Not applicable.

Data Availability Statement: Data is unavailable due to privacy or ethical restrictions.

Conflicts of Interest: The authors declare no conflict of interest.

Abbreviations

SAD	secondary aluminum dross
WFA	waste fly ash
UHPC	ultra-high-performance concrete
DSR	dry shrinkage rate
EDS	electron microscopy spectroscopy
TG	thermogravimetric analysis
XRD	X-ray diffraction spectrum
SEM	scanning electron microscopy
DSR	drying shrinkage rate
L_0	initial lengths
L_t	length
C-S-H	calcium silicate hydrate
CH	Ca(OH)_2
C3S	$3\text{CaO}\cdot\text{SiO}_2$
C2S	$2\text{CaO}\cdot\text{SiO}_2$

References

- Liu, B.; Meng, H.; Pan, G.H.; Zhou, H. Relationship between the fineness and specific surface area of iron tailing powder and its effect on compressive strength and drying shrinkage of cement composites. *Constr. Build. Mater.* **2022**, *357*, 129421. [[CrossRef](#)]
- Avila-López, U.; Almanza-Robles, J.M.; Escalante-García, J. Investigation of novel waste glass and limestone binders using statistical methods. *Constr. Build. Mater.* **2015**, *82*, 296–303. [[CrossRef](#)]
- Alderete, N.; Joseph, A.; Van den Heede, P.; Matthys, S.; De Belie, N. Effective and sustainable use of municipal solid waste incineration bottom ash in concrete regarding strength and durability. *Resour. Conserv. Recycl.* **2021**, *167*, 105356. [[CrossRef](#)]
- Mandpe, A.; Yadav, N.; Paliya, S.; Tyagi, L.; Yadav, B.R.; Singh, L.; Kumar, S.; Kumar, R. Exploring the synergic effect of fly ash and garbage enzymes on biotransformation of organic wastes in in-vessel composting system. *Bioresour. Technol.* **2021**, *322*, 124557. [[CrossRef](#)] [[PubMed](#)]
- Ramesh Kumar, G.; Bharani, S.; Anupriya, R.; Jeevitha, V.; Gnanajothi, G. Influence of electronic waste and fly ash in strength and durability properties of concrete. *Mater. Today Proc.* **2022**, *62*, 2230–2234. [[CrossRef](#)]
- Cui, L.; Wang, H. Influence of Waste Fly Ash on the Rheological Properties of Fresh Cement Paste and the Following Electrical Performances and Mechanical Strengths of Hardened Specimens. *Coatings* **2021**, *11*, 1558. [[CrossRef](#)]
- Du, Y.; Hao, W.; Shi, F.; Wang, H.; Xu, F.; Du, T. Investigations of the Mechanical Properties and Durability of Reactive Powder Concrete Containing Waste Fly Ash. *Buildings* **2022**, *12*, 560. [[CrossRef](#)]
- David, O.; Opeyemi, J.; Adekunle, M.; Babatunde, F. Influence of secondary aluminum dross (SAD) on compressive strength and water absorption capacity properties of sandcrete block. *Cogent. Eng.* **2019**, *6*, 1608687.
- Panditharadhya, B.J.; Sampath, V.; Shankar, A.U.R. Mechanical properties of pavement quality concrete with secondary aluminium dross as partial replacement for ordinary portland cement. *Mater. Sci. Eng.* **2018**, *431*, 032011. [[CrossRef](#)]
- Satish, R.; Neeraja, D. Mechanical and durability aspects of concrete incorporating secondary aluminium slag. *Resour.-Effic. Technol.* **2016**, *2*, 225–232.
- Ewais, E.M.M.; Khalil, N.M.; Amin, M.S. Utilization of aluminum sludge and aluminum slag (dross) for the manufacture of calcium aluminate cement. *Ceram. Int.* **2009**, *35*, 3381–3388. [[CrossRef](#)]
- Zhang, Y.; Guo, C.H. Effects of AlN hydrolysis on fractal geometry characteristics of residue from secondary aluminium dross using response surface methodology. *T. Nonferr. Metal. Soc.* **2018**, *28*, 2574–2581. [[CrossRef](#)]
- Arimanwa, J.I.; Onwuka, D.O.; Arimanwa, M.C.; Onwuka, U.S. Prediction of the compressive strength of aluminum waste–cement concrete using Scheffe's theory. *J. Mater. Civ. Eng.* **2012**, *24*, 177–183. [[CrossRef](#)]
- Ren, Y.C.; Wu, F.H.; Qu, G.F. Extraction and preparation of metal organic frameworks from secondary aluminum ash for removal mechanism study of fluoride in waste water. *J. Mater. Res. Technol.* **2023**, *23*, 3023–3034. [[CrossRef](#)]
- Trinet, Y. The influence of aluminum dross on mechanical and corrosion properties of cement paste: PART I. *Eng. Technol.* **2019**, *10*, 192–201.
- Sharma, R.; Kim, H.; Pei, J.; Jang, J.G. Dimensional stability of belite-rich cement subject to early carbonation curing. *J. Build. Eng.* **2023**, *63*, 105545. [[CrossRef](#)]
- IV, G.M.; Sinnan, R.; Young, M. Evaluation of reclaimed municipal solid waste incinerator sands in concrete. *J. Cleaner Prod.* **2019**, *229*, 838–849.
- Miguel, F.; Brito, J.D.; Silva, R.V. Durability-related performance of recycled aggregate concrete containing alkali-activated municipal solid waste incinerator bottom ash. *Const. Build. Mater.* **2023**, *397*, 132415. [[CrossRef](#)]

19. Elseknidy, M.; Salmiaton, A. A Study on Mechanical Properties of Concrete Incorporating Aluminum Dross, Fly Ash, and Quarry Dust. *Sustainability* **2020**, *12*, 9230. [[CrossRef](#)]
20. Gireesh, M.; Sujay, R.; Sreedhara, B.M.; Manu, D.S. Investigation of concrete produced using recycled aluminium dross for hot weather concreting conditions. *Resour.-Effic. Technol.* **2016**, *2*, 68–80.
21. Suescum-Morales, D.; Silva, R.V.; Bravo, M.; Jiménez, J.R.; Fernández-Rodríguez, J.M.; Brito, J.D. Effect of incorporating municipal solid waste incinerated bottom ash in alkali-activated fly ash concrete subjected to accelerated CO₂ curing. *J. Clean. Prod.* **2022**, *370*, 133533. [[CrossRef](#)]
22. Liu, B.; Yang, L.; Shi, J.; Zhang, S.; Yaçınkaya, Ç.; Alsharif, A.F. Effect of curing regime on the immobilization of municipal solid waste incineration fly ash in sustainable cement mortar. *Environ. Pollut.* **2023**, *317*, 120839. [[CrossRef](#)] [[PubMed](#)]
23. Wang, H.; Jin, K.; Zhang, A.; Zhang, L.; Han, Y.; Liu, J.; Shi, F.; Feng, L. External erosion of sodium chloride on the degradation of self-sensing and mechanical properties of aligned stainless steel fiber reinforced reactive powder concrete. *Constr. Build. Mater.* **2021**, *287*, 06629. [[CrossRef](#)]
24. Moini, R.; Olek, J.; Zavattieri, P.D.; Youngblood, J.P. Early-age buildability-rheological properties relationship in additively manufactured cement paste hollow cylinders. *Cem. Concr. Compos.* **2022**, *131*, 104538. [[CrossRef](#)]
25. Athira, G.; Bahurudeen, A. Rheological properties of cement paste blended with sugarcane bagasse ash and rice straw ash. *Constr. Build. Mater.* **2022**, *332*, 127377. [[CrossRef](#)]
26. Gupta, S.; Mahmood, A.H. A multi-method investigation into rheological properties, hydration, and early-age strength of cement composites with admixtures recovered from inorganic and bio-based waste streams. *Constr. Build. Mater.* **2022**, *347*, 128529. [[CrossRef](#)]
27. Wang, H.; Shen, J.; Liu, J.; Lu, S.; He, G. Influence of carbon nanofiber content and sodium chloride solution on the stability of resistance and the following self-sensing performance of carbon nanofiber cement paste. *Case Stud. Constr. Mater.* **2019**, *11*, e00247. [[CrossRef](#)]
28. Zhang, Y.B.; Lin, K.; Su, Z.J. Self-driven hydrolysis mechanism of secondary aluminum dross (SAD) in the hydrometallurgical process without any additives. *Chem. Eng. J.* **2023**, *466*, 143141. [[CrossRef](#)]
29. Lucía, G.; Miguel, Á.V. Synthesis strategies of alumina from aluminum saline slags. *Process Saf. Environ. Prot.* **2023**, *172*, 1010–1028.
30. Gou, J.; Wang, G.; Al-Tamimi, H.; Alkhalifah, T.; Alturise, F.; Ali, H.E. Application of aluminum oxide nanoparticles in asphalt cement toward non-polluted green environment using linear regression. *Chemosphere* **2023**, *321*, 137925. [[CrossRef](#)]
31. Ayobami, B.; Jacques, S.; Williams, K. Data on the engineering properties of aluminum dross as a filler in asphalt. *Data. Brief.* **2020**, *31*, 105934.
32. Elinwa, A.U.; Mbadike, E. The use of aluminium waste for concrete production. *J. Asian Arch. Build. Eng.* **2011**, *10*, 217–220. [[CrossRef](#)]
33. Ozerkan, N.G.; Maki, O.L.; Anayeh, M.W.; Tangen, S. The effect of aluminium dross on mechanical and corrosion properties of concrete. *Int. J. Innov. Res. Sci. Eng. Technol.* **2014**, *3*, 9912–9922.
34. Paktiawal, A.; Alam, M. An experimental study on effect of aluminum composite panel waste on performance of cement concrete. *Ain. Shams. Eng. J.* **2021**, *12*, 83–98. [[CrossRef](#)]
35. Xu, W.; Wang, H.; Tian, X. The Effect of Secondary Aluminum Ash on the Properties of Reactive Powder Concrete. *Materials* **2023**, *16*, 5265. [[CrossRef](#)]
36. Hang, T.; Luca, S.; David, B. Development of sustainable ultra-high performance concrete recycling aluminum production waste. *Constr. Build. Mater.* **2023**, *371*, 130212.
37. Li, P.; Guo, M.; Zhang, M.; Teng, L.D. Leaching Process Investigation of Secondary Aluminum Dross: The Effect of CO₂ on Leaching Process of Salt Cake from Aluminum Remelting Process. *Metall. Mater. Trans. B* **2012**, *43*, 1220–1230. [[CrossRef](#)]
38. Haneef, S.M.; Harish, P. An Experimental Investigation on Use of Secondary Aluminium Dross in Cement Concrete. *Eng. Technol.* **2016**, *2*, 204–207.
39. Pereira, D.A.; De, A.B.; Castro, F. Mechanical behaviour of Portland cement mortars with incorporation of Al-containing salt slags. *Cem. Concr. Res.* **2000**, *30*, 1131–1138. [[CrossRef](#)]
40. Nduka, D.; Ede, A. Mechanical and Water Absorption Properties of Normal Strength Concrete (NSC) Containing Secondary Aluminum Dross (SAD). *Int. J. Eng. Res. Afr.* **2020**, *47*, 1–13. [[CrossRef](#)]
41. Xu, L.; Li, X.B.; Liu, Y.; Chen, M.; Wang, N. Recovery of low phosphorus iron from steel slag using secondary aluminum dross as the reductant. *J. Environ. Chem. Eng.* **2023**, *11*, 110973. [[CrossRef](#)]
42. Mahinroosta, M.; Allahverdi, A. Enhanced alumina recovery from secondary aluminum dross for high purity nanostructured γ -alumina powder production: Kinetic study. *J. Environ. Manag.* **2018**, *212*, 278–291. [[CrossRef](#)] [[PubMed](#)]
43. Xu, J.; Wang, H.; Wang, W.; Shi, F. The Influence of CO₂-Cured Incinerated Waste Fly Ash on the Performance of Reactive Powder Concrete. *Coatings* **2023**, *13*, 709. [[CrossRef](#)]

Disclaimer/Publisher’s Note: The statements, opinions and data contained in all publications are solely those of the individual author(s) and contributor(s) and not of MDPI and/or the editor(s). MDPI and/or the editor(s) disclaim responsibility for any injury to people or property resulting from any ideas, methods, instructions or products referred to in the content.